AAS 21-290

CISLUNAR SPACE SITUATIONAL AWARENESS

Carolin Frueh*, Kathleen Howell†, Kyle J. DeMars‡, Surabhi Bhadauria§

Classically, space situational awareness (SSA) and space traffic management (STM) focus on the near-Earth region, which is highly populated by satellites and space debris objects. With the expansion of space activities further in the cislunar space, the problems of SSA and STM arise anew in regions far away from the near-Earth realm. This paper investigates the conditions for successful Space Situational Awareness and Space Traffic Management in the cislunar region by drawing a direct comparison to the known challenges and solutions in the near-Earth realm, highlighting similarities and differences and their implications on Space Traffic Management engineering solutions.

INTRODUCTION

Space Situational Awareness (SSA), sometimes called Space Domain Awareness (SDA), can be understood as summary terms for the comprehensive knowledge on all objects in a specific region without necessarily having direct communication to those objects. Space Traffic Management (STM), as an extrapolatory term, is applying the SSA knowledge to manage this said region to enable sustainable use. All three of those terms have traditionally been applied to the realm of the near-Earth space, usually expanding from low Earth orbit (LEO) to hyper geostationary orbit (hyper-GEO), and the objects of interest are objects in orbital motion for which the dominant astrodynamical term is the central gravitational potential of the Earth. Space Traffic Management (STM) aims at engineering solutions, methods, and protocols that allow regulating space fairing in a manner enabling the sustainable use of space. SSA and SDA thereby provide the knowledge-base for STM, and the areas are heavily intertwined.

Regular space fairing is expanding into the cislunar realm – the space from hyper-GEO all the way to the Moon – and emerges as the new frontier in space regarding commercial, space exploratory and experimental, and defense interests [1, 2, 3]. With new and old spacecrafts, aging effects, and inevitably, space debris, this is creating a situation comparable to the highly populated near-Earth region and generates the need for cislunar space situational awareness (CSSA), Cislunar Domain Awareness (CDA), and cislunar space traffic management (CSTM) to allow for the sustainable long term usability of the region.

In order to achieve CSSA/CSA and CSTM, the aforementioned tasks have to be expanded beyond the geosynchronous orbit to the vast cislunar region. In the cislunar realm, apart from the near-Lunar region, the dynamical environment is different with small accelerations that are not necessarily directed towards a single central gravitational body. One of the challenges is that this expansion requires new metrics and evaluation criteria even to start gauging the problem of such an expansion [4]. The increased distances to the Earth pose challenges for observation collection, and communication, as well as for satellite operation in the absence of Global Positioning System (GPS) (although it should be noted that in the near-Lunar region, concepts for GPS-like constellations are being discussed [5]). Alternative communication structures have been proposed [6]. Some research on CSSA and CSTM has focused on the use of on-orbit optical telescopes to aid in establishing an observational basis for some of the popular cislunar orbits, such as [7] and [8], or to explore a heterogeneous setup of a variety of sensors, combining space-based and ground-based assets [9]. Orbital

*Associate Professor, School of Aeronautics and Astronautics, 701 W. Stadium Avenue, Lafayette, IN 47907.
†Professor, School of Aeronautics and Astronautics, 701 W. Stadium Avenue, Lafayette, IN 47907.
‡Associate Professor, Department of Aerospace Engineering, Texas A&M University, College Station, TX 77843.
§Graduate Student, School of Aeronautics and Astronautics, 701 W. Stadium Avenue, Lafayette, IN 47907.

propagation needs to be significantly expanded and coupled with interplanetary techniques, with the first steps being made in this direction [10]. Because of the changed dynamical environment, orbit determination techniques need to be significantly adapted in order to be successful in the cislunar realm, such as based on optical observations alone [11, 12], e.g., for satellite navigation.

In this paper, we want to illustrate the concept of exploring orbital families for orbit selection, the effect of the different propagation models and coordinate frames and forces, the ground coverage for optical observations under various constraints, and the uncertainty propagation in the cislunar realm. For this purpose, three different types of orbits are introduced, the Distant Retrograde Orbit (DRO) orbit family, and the Lyapunov orbital family, and a transfer orbit from the Earth to an L_2 halo orbit. From the latter two, one sample orbit is selected for ground-coverage, uncertainty propagation investigations. In terms of propagation models, the circular restricted three body propagation is compared with different numerical propagation models of various fidelities. As for coordinate frames, the rotating coordinate frame and the inertial J2000.0 frame are used.

THE CISLUNAR DYNAMICAL ENVIRONMENT

In the following, the force environment in the cislunar space is illustrated in order to provide a comparison to the near-Earth region. For the illustration, the accelerations experienced by a space object are computed throughout the cislunar realm.

For the acceleration computation, a reference date, March 20, 2020, at midnight UTC, has been used. The forces that have been taken into account for the simulation are the Earth gravitational potential, explicated out in the central potential and J2 term, the solar and lunar point mass gravitational force, Jupiter's gravitational force, solar radiation pressure, and drag in the altitude up to 1000 km from the Earth's surface. The parameters for the solar radiation pressure, an area-to-mass ratio of 0.02 m^2/kg is assumed (a standard value corresponding e.g., to a GPS satellite) with a diffuse reflection parameter of $C_d = 0.8$ and a one-meter diameter in a cannonball model. Drag is computed via the circular orbit velocity at the given location.

Fig. 1a shows the combined accelerations due to all the aforementioned forces except drag. One can clearly see the gravitational wells created by the Earth and the Moon. Selecting the color cording to a yellow cutoff of 0.009 m/s^2, illustrates the variety of accelerations present in the cislunar region that is far from being completely flat. Figs. 1b and 1c are singling out the accelerations due to Jupiter, which can be seen to be behind the Moon at the time of the acceleration, and the solar radiation pressure, which shows the cross-related accelerations from the Sun. Naturally, the solar radiation pressure acceleration with an opposed direction indicates the direction of the solar gravity.

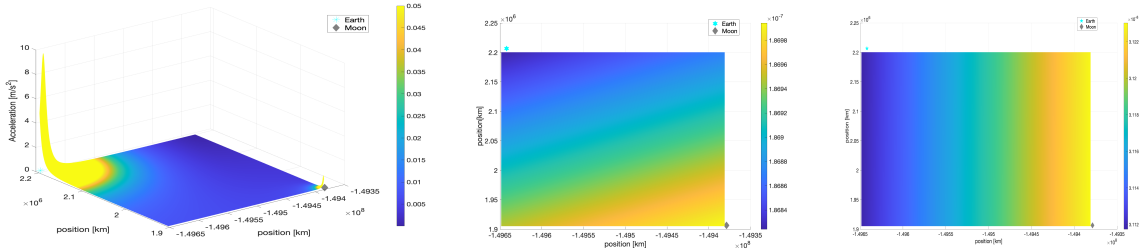

(a) All accelerations (b) Jupiter (c) Solar radiation pressure

Figure 1: Accelerations due to a) combined accelerations due Earth, solar, lunar and Jupiter gravity and solar radiation pressure b) Jupiter and c) solar radiation pressure as a function of position, the colorbar indicates accelerations in $\frac{m}{s^2}$.

This can be compared to the situation in the near-Earth environment. In the near-Earth environment, the dominant term is Earth gravitational potential with its strongest central term, followed by drag and or higher-order gravitational terms, depending on the satellite layout. When focusing on the acceleration direction,

it is clear that the dominant direction points towards the central body, even in the presence of drag. Only extremely high area-to-mass ratio objects could force objects into significant deviations from a central body acceleration sometimes referred to as displaced orbits [13].

CIRCULAR RESTRICTED THREE BODY PROBLEM, COORDINATE FRAMES, AND PROPAGATION MODELS

The Circular Restricted Three-Body Problem (CR3BP) model is useful for preliminary analysis of trajectories in the Earth-Moon system. The motion of a spacecraft, assumed with a negligible mass, is governed by both the Earth and the Moon's gravitational forces simultaneously. The Earth and the Moon are termed the primaries P_1 (mass m_1) and P_2 (mass m_2), respectively. The primaries are assumed to move on circular orbits relative to the system barycenter (BA). The barycentric rotating frame, R, is defined such that the rotating x-axis is directed from the Earth to the Moon, the z-axis is parallel to the direction of the orbital angular momentum of the primary system, and the y-axis completes the orthonormal triad. The state vector $\boldsymbol{x} = [x, y, z, \dot{x}, \dot{y}, \dot{z}]^T$ for the spacecraft relative to the Earth-Moon barycenter is defined in terms of the rotating coordinates. By convention, quantities in the CR3BP are non-dimensional such that, firstly, the characteristic length is the distance between the Earth and the Moon. Secondly, the characteristic mass is the sum $m_1 + m_2$, and thirdly, the characteristic time is determined such that the non-dimensional gravitational constant is equal to unity.

The mass parameter is then defined as $\mu = \frac{m_2}{m_1+m_2}$. The first order non-dimensional equation of motion in vector form is then:

$$\dot{\boldsymbol{x}} = \boldsymbol{f}(\boldsymbol{x}), \tag{1}$$

with the vector field

$$\boldsymbol{f}(\boldsymbol{x}) = [\dot{x}, \dot{y}, \dot{z}, 2n\dot{y} + U_x, -2n\dot{x} + U_y, U_z]^T, \tag{2}$$

where n denotes the non-dimensional mean motion of the primary system. The vector field is expressed in terms of the pseudo-potential function:

$$U(x, y, z, n) = \frac{1-u}{d} + \frac{\mu}{r} + \frac{1}{2}n^2(x^2 + y^2), \tag{3}$$

where the non-dimensional quantities d and r denote the Earth-spacecraft and Moon-spacecraft distances, respectively. The quantities U_x, U_y, and U_z represent the partial derivatives of the pseudo-potential function with respect to the rotating position coordinates. Only one integral of motion is known to exist, named the Jacobi constant, C, which is evaluated as:

$$C = 2U - v^2 \qquad \text{with} \qquad v = \sqrt{\dot{x}^2 + \dot{y}^2 + \dot{z}^2} \tag{4}$$

The Jacobi constant is a constant of motion in the rotating frame. It offers useful information concerning the energy level associated with a periodic orbit or a trajectory arc in the CR3BP.

For visual interpretation and clarity, it is frequently convenient to view the trajectories in the inertial frame. A transformation from rotating to inertial coordinates is easily accomplished. An inertial frame, I, with the coordinate directions denoted by $\hat{X}, \hat{Y}, \hat{Z}$ and the rotating frame R are related such that the angular velocity of the rotating frame relative to the inertial frame is $\omega := n\hat{z} = n\hat{Z}$. Under the assumption of the CR3BP, the mean motion n is constant and can be expressed as $n = \dot{\theta}$, with the angular velocity $\dot{\theta}$. With the non-dimensional value $n = 1$, it is observed that the angle θ ranges from 0 to 2π over each revolution of the Earth-Moon system in the inertial frame. The inertial frame is defined as the J2000.0 reference frame in its classical form centered on the Earth.

In the course of this paper, for precise orbit propagation, two models are used utilizing numeric integration in the inertial J2000.0 frame (centered on the Earth) in Cartesian Coordinates. For a simple comparison to the CR3BP, first, a *simplified dynamics model* is used, in which only the point gravity of the Earth and the Moon

is taken into account with a simplified lunar position. In the *full ephemerides model*, the Earth gravitational potential, including the main harmonic terms of (2,0) (2,2) (3,0) (3,1) (4,0) and the point gravitational sources of the Sun, the Moon and Jupiter, and SRP have been taken into account. For the Jupiter's, lunar, and solar position, precise SPICE ephemerides are used. The solar radiation pressure model is a cannonball model with a one-meter diameter with a diffuse reflection coefficient of 0.5 and an area-to-mass ratio of 0.02 m^2/kg.

ORBIT SELECTION

As is apparent from the preliminary analysis, accelerations throughout the cislunar region are much more variable than in the near-Earth domain. Such variability offers a much broader array of orbits and transfer paths throughout the region. A number of orbital families, for example, are not available under a two-body or conic model. Rather, some less familiar orbital families emerge with different types of characteristics to be leveraged for new types of activities. Conversely, this variation also delivers new challenges for efforts to support orbital catalogs and predictions of behaviors in this regime. In an effort to explore the challenges, some orbits are selected to examine the acceleration levels as well as prediction. The sample obits for some preliminary analysis include Distant Retrograde orbits (DROs) and Lyapunov orbits. In addition, a transfer orbit is introduced as a type or orbital path through the entire cislunar region.

resonant orbits are introduced as some options that will flow, over time, through the entire cislunar region.

Earth-Moon Distant Retrogrades Orbits (DROs)

Distant retrograde orbits, or DROs, have been the focus of much discussion recently due to the inherent linear stability of the many of the DROs. These orbits are precisely periodic in the CR3BP but generally retain their characteristics when transitioned to an ephemerides model. A family of planar DROs ranges throughout the region and encompasses the Earth-Moon L_1 and L_2 libration points. Each family in the CR3BP includes an infinite number of members that can be distinguished by a number of factors including period and energy level. Some of these orbits pass near the Earth and then the far side of the Moon. It is also true that there are members that pass nearly through the L_1 and L_2 libration points. A subset of the family of distant retrograde orbits is plotted in Fig. 2a. Note the direction of motion. One member of the family is highlighted in black; it is the sample orbit chosen for further exploration. This orbit has been selected for its properties to inhabit the cislunar region between the Earth and the Moon, with the passage outside the libration points.

For the propagation, the CR3BP and the simple ephemerides model is used. The orbit has been propagated for about 26.22 days, the start epoch is MJD 58849.0 (Jan 1 20202, 0h). The propagation model influences the orbital development, as the comparison in Fig. 2b shows, however, the general shape of the orbit is preserved even using a simpler ephemerides model. This is the case because the DRO unfolds in the middle region between the Earth and the Moon, where smaller accelerations are dominating, as described in the previous section. Of course, a corrections process can be implemented in the ephemerides model to retain specific characteristics if required [14, 15].

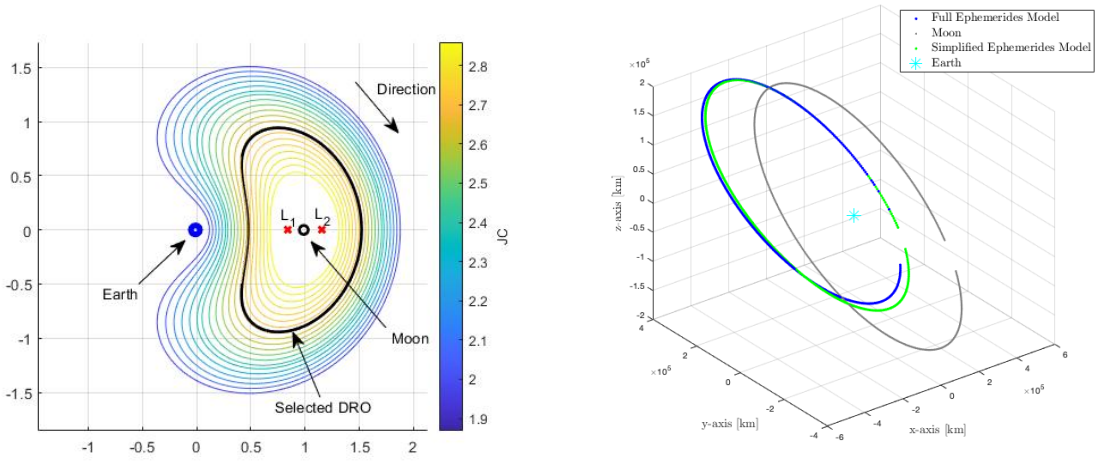

(a) DRO Orbital Family, Rotating Frame

(b) Selected DRO, Inertial Frame

Figure 2: a) Family of precisely periodic Distant Retrograde Orbits (DROs) in the CR3BP. Colors indicate the energy range in terms of the Jacobi Constant. One member of the family is selected (black) that passes nearly halfway between the Earth and the Moon. b) the selected DRO orbit propagated with the two different dynamical models (green simplified dynamics, blue full ephemerides model) in the inertial J2000.0 frame.

Earth-Moon Lyapunov Orbits

A planar family of Lyapunov orbits originates in the vicinity of each of the Earth-Moon collinear libration points. Consistent with DROs, the Lyapunov orbits are precisely periodic in the CR3BP and also retain their general characteristics when transitioned to an ephemerides model. Each family in the CR3BP includes an infinite number of members, distinguished by a number of factors including period and energy level. In the Earth-Moon system, a portion of the L_1 family of Lyapunov orbits is plotted in Fig. 3a. The family extends all the way to the Earth. The family member that has a close lunar passage is selected for further investigation. It is an orbit that covers the cislunar space, but the close lunar passage would allow for lunar surveillance or interaction with lunar orbiters; a characteristic which is interesting for current and future missions.

The propagation model has significant influence on the orbital development, as the comparison in Fig. 3b shows, the time over which the orbit has been propagated is about 32.07 days, the start epoch is MJD 58849.0 (Jan 1 20202, 0h). The simplified dynamics model neglects the lunar gravity, which has a huge effect on the orbit because of the close lunar fly-by and leads to a sharp point of departure after about half of the orbital period. Using the higher fidelity model, where besides the gravitational potential of all three main bodies, Earth, Sun and Moon, also SRP is taking into account, a much smoother trajectory is reached.

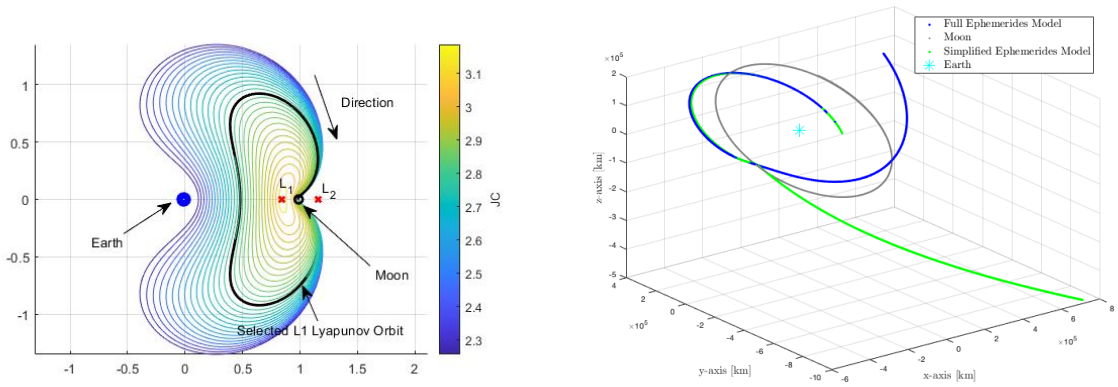

(a) Lyapunov Orbital Family, Rotating Frame

(b) Selected Lyapunov orbit, Inertial Frame

Figure 3: a) A family of L_1 Lyapunov orbits in the Earth-Moon CR3BP. Colors indicate the energy range in terms of the Jacobi Constant. One member of the family is selected (black) that passes relatively close to the Moon. b) the selected Lyapunov orbit propagated with the two different dynamical models (green simplified dynamics, blue full ephemerides model) in the inertial J2000.0 frame.

The Earth-L_2 Halo Transfer Orbit

To investigate a different type of orbit in the cislunar regime, a transfer orbit is constructed from LEO to a three-dimensional L_2 southern halo orbit [16, 17]. A projection of the transfer onto the x-y plane appears in Fig. 4. The departure orbit is circular and 210 km altitude. The arrival L_2 southern halo orbit possesses a period of 14.77 days; A member of the L_2 halo family, the Jacobi constant value corresponding to this orbit is JC = 3.13713. As apparent in the figure, the transfer includes two maneuvers, one to depart the Earth orbit and one to insert onto the halo orbit stable manifold. The Earth departure maneuver is quite standard; the insertion maneuver at nearly 700 m/s has not been optimized and serves as a suitable initial guess for such a transfer. Consistent with the previous CR3BP orbits, the initial states for the transfer were straightforwardly used in the two different dynamics models and propagated forward in time without any attempt to update the state prior to propagation and the resulting paths are plotted in Fig. 5. This is the resulting orbit without inclusion of the second maneuver. As a result, the orbit loops back to the Earth after the lunar passage. Employing a corrections process, the transfer would blend smoothly and, with a updated maneuver, flow into the L_2 orbit if this effort was focused upon a transfer. Rather, in this analysis, the path is employed to assess surveillance capabilities; as such, the propagated arcs are sufficient.

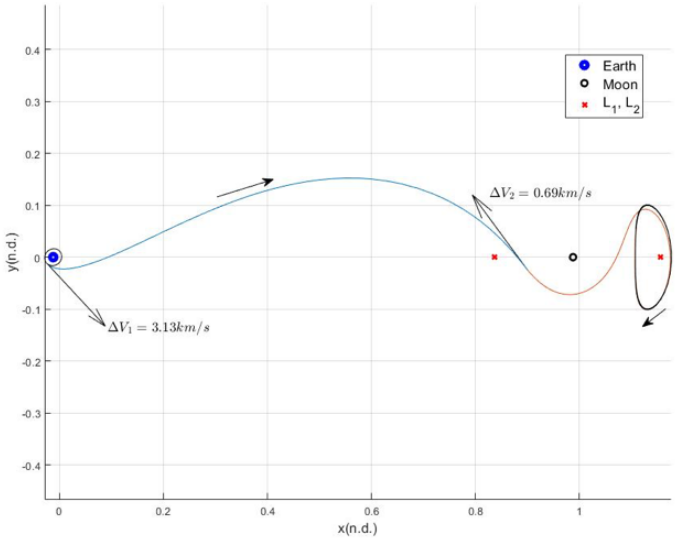

Figure 4: Transfer orbit between LEO and an L_2 southern halo orbit in the Earth-Moon CR3BP.

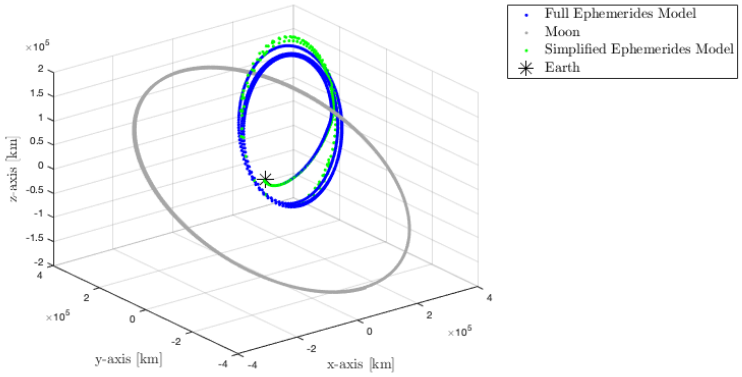

Figure 5: The selected Transfer orbit propagated with the two different dynamic models, simplified dynamics and full ephemerides model in the inertial J2000.0 frame, just after the first maneuver.

SURVEILLANCE OF THE SELECTED CISLUNAR ORBITS

One of the key elements in cislunar Space Surveillance is the coverage with observations. One of the challenges are the large distances to the objects in the cislunar space. In this paper, the focus is on ground based optical measurements. Those sensors are not the best suited ones, but the ones most widely available. For complete surveillance, supplementation of sensors on the Moon and on cislunar orbits are required.

In order to model the optical sensor, the magnitude of a representative space object on the selected sample orbits is computed. The magnitude of a space object is:

$$\text{mag} = \text{mag}_{\text{sun}} - 2.5 \log_{10}(\frac{I_{\text{sc}}}{I_{\text{sun}}}) \tag{5}$$

where mag_{sun} is the apparent reference magnitude of the Sun, I_{sc} is the irradiance reflected off the spacecraft and I_{Sun} is the Sun's reference irradiance. In order to compute the irradiance that is reflected off the object,

an assumption about the albedo-area, the shape and attitude of the space object has to be made. In this paper, we assume, in agreement with the solar radiation pressure modelling of a spherical object. This is a good baseline scenario. Overall, for satellites in a box wing configuration, higher irradiation is received in the case of a specular glint off the solar panels or the antennas. However, those glints are, per definition, not continuous and only occur during very limited times over one period, if at all, depending on the Sun-object-observer geometry. A Lambertian sphere on the other hand has the advantage of, other than in the time of complete opposition, always reflecting a fraction of the Sun's irradiation towards the observer; a fact not given for a non-spherical object. In future work, the exact orientation of a given satellite configuration will be evaluated. The irradiance of the object can hence be expressed via the the following relation [18]:

$$I_{\mathrm{sc}} = \frac{I_{\mathrm{Sun}}}{d^2_{\mathrm{sc_{obs}}}} \frac{2}{3} \frac{C_d}{\pi^2} r^2 (\sin\alpha + (\pi - \alpha)\cos\alpha) \tag{6}$$

$d_{\mathrm{sc_{obs}}}$ is the distance between the object and the observer, r is the object's radius, and α is the phase angle between the Sun and the observer at the object's location. It is important to note that the solar constant I_0, needs to be scaled to the actual distance between the Sun and the object $d_{\mathrm{Sun_{sc}}}$ for the reference irradiance $I_{\mathrm{Sun}} = I_0 \frac{\mathrm{AU}^2}{d^2_{\mathrm{Sun_{sc}}}}$ as the solar constant is defined at one Astronomical Unit (AU). This is relevant when computing the absolute irradiation of the object.

For the visibility besides the overall magnitude also the background irradiation entering the sensor are relevant, creating the so-called detection signal to noise ratio (SNR) in its definition mean divided by the standard deviation [19]:

$$\mathrm{SNR} = \frac{S}{\sqrt{S+N}}, \tag{7}$$

Where S and N denote the mean (and variance) of the Poisson distributed signal of interest and the noise, respectively. The signal of interest is in our case the signal contained in the object image on the detector and the noise is in those same pixels.

The detection limit is directly dependent on the SNR and is dictated by the exact setup of optic's aperture, sensor type and sensitivity in combination with the specific image processing software. While, for methodologies employing stacking, detection limits can be pressed to be below an SNR of 1, this requires precise tracking and is inversely proportional to the time spent on observing the object, which is not realistic or feasibile in many cases. In this paper, a realistic more general signal dependent threshold of $SNR = \sqrt{S/2}$ is used.

Night time visibility constraints are often listed as a separate observation constraint, however, strictly speaking, night time constraints are also SNR constraints. Daytime imaging of satellites in off-Sun directions is possible, however, the higher background requires a much higher object magnitude to reach the same SNR. In general, daytime observations require magnitudes of 8 and brighter. In the investigations shown in this paper, none of the observation reached this magnitude, and brightest magnitudes are of the order of 14 and higher. For this reason, night time constraints are applied, requiring observations to take place after astronomical sunset. For the SNR a limit of $\sqrt{S/2}$ is used, which serves as a lower bound.

One of the most relevant background sources for cislunar observations is the lunar background, as observation directions close to the moon are more frequent. The lunar stray light is computed for each viewing direction [20].

Besides the SNR, visiblity constraints include, as the observations are assumed to be ground-based, local weather and local horizon constraints. The weather is highly variable and not taken into account here. A local horizon constraint of 0 degrees above horizon has be employed, again serving as the lower limit.

The Seleted DRO

For the selected DRO orbit, Fig. 6 shows the magnitudes as a function of the time, measured from midnight Jan 1, 2020 in hours, for various C_d values (see Eq. 6), local horizon constraints. The radius of the sphere

is assumed to be 3.54 meters. The black bars indicate background night time sky's moon brightness in the viewing direction to the object when observed from a station located at latitude = 40.4310 degrees North and Longitude 86.9149 East. The gray bars indicate the night time, during which observations are possible. The lowest magnitude is reached at all times, by the sphere with the highest reflectivity, of course. What is shown is that the moons background brightness significantly interferes with the observations from around 200 to 300 hours. Overall, with a telescope with limiting magnitude of 16 only a fraction of the orbit can be covered with observations even for the most reflective objects, at the beginning of the time interval and after 650 hours.

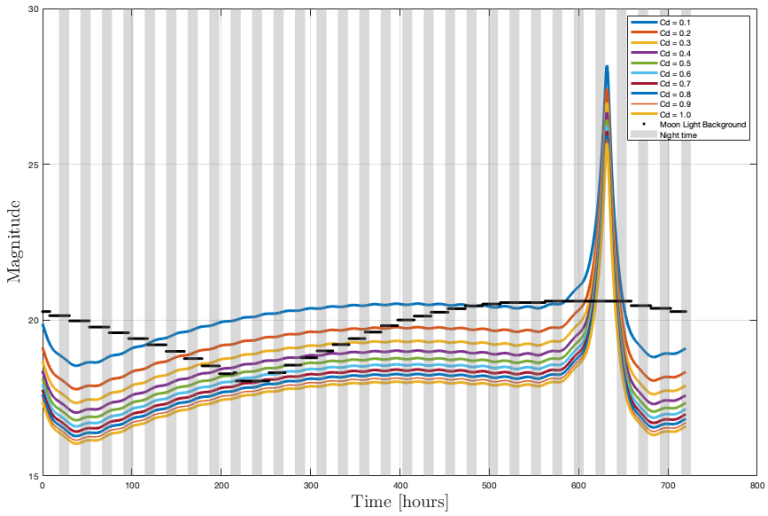

Figure 6: The selected DRO: Magnitude of a 3.54 meter radius object as a function of time. The Sky brightness solely based on the Moon in the viewing direction is shown with the observation location at about 40.4 deg N, 86.9 E.

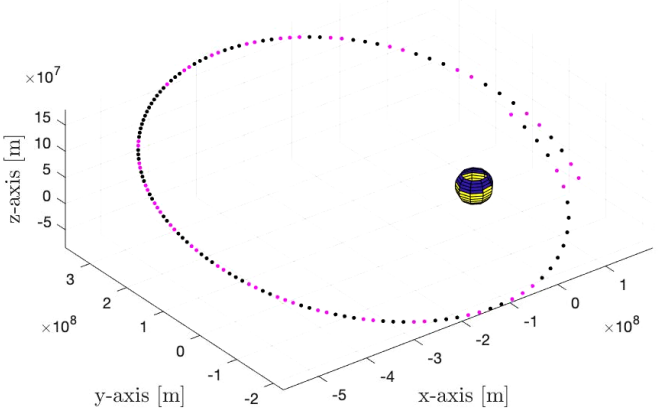

Figure 7: The selected DRO: Trajectory of the object and visibilities for a ground-based observer with a limiting magnitude of 20 and lunar background light, for a 1.8 meter radius object and $C_d = 0.5$ and a minimum elevation of zero degrees. Ground-based sensor locations with visiblities are yellow, the ones without are marked in blue (Earth size not to scale), the trajectory, for which at least one ground-based sensor has a visibility is marked pink, otherwise blue.

The detectability of the object, not surprisingly, is highly dependent upon the location on the Earth, where the sensor is located. Fig. 7 shows the visibility of the DRO a 1.8 meter radius object with a reflection coefficient $C_d = 0.5$, constrained to a zero elevation angle along with magnitude of the object that is larger than the Moon-induced background sky brightness with the $SNR = \sqrt{S/2}$ constraint and a limiting magnitude of 20. The orbit which can be covered by observation located at the center of each Earth grid point is marked in pink and the corresponding sensor locations in yellow. Regions with no observation coverage by any earth sensor location is marked in black. More than in near-Earth surveillance, it is obvious a global network of sensors is not optional. Furthermore, even with a global coverage, certain observation gaps exist, most significantly at regions after completing about half of the orbital period, in the region farthest from the earth. However, even when the object is closer, e.g. because of illumination conditions, visibility is not guaranteed, see Fig.7.

The Selected Lyapunov Orbit

For the selected Lyapunov orbit, the same magnitude calculations have been performed for various C_d reflection coefficients for a spherical object with a radius of 3.54 meters, see Fig. 8. The ground-based observer has been placed again at latitude = 40.4310 degrees North and Longitude 86.9149 degrees East. Shown are the night times via gray bars and the background moon light's magnitude in the viewing direction to the object in black.

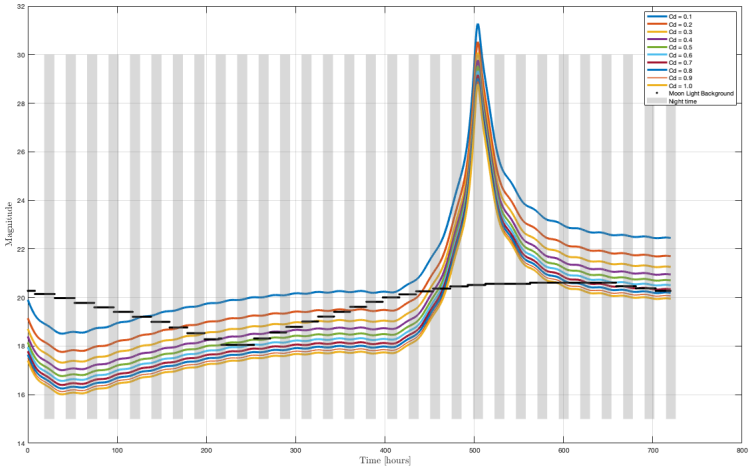

Figure 8: The selected Lyapunov orbit: Magnitude of a one 3.54 meter radius object as a function of time with the observation location at about 40.4 deg N, 86.9 deg E.

Because the magnitude is largely dominated by the distance between the object and the observer, for a sensor with a limiting magnitude of 16, one has only the early part of the trajectory to allow for observations, even with a sensor as sensitive as magnitude 20, only barely the last part of the orbit is allowed for observations. As the distance to the earth has significantly increased, no lower magnitudes are reached even for the most reflective objects. At the region, where the object is farthest from the earth, around 500 hours, in combination with the phase angle, no observations are possible, with the object becoming as faint as magnitude 30. Towards the end of the propagation period, the object stays faint while also the moonlight thwarts any observation possibility. This is comparable to other sensor locations, as shown in Fig. 9.

Fig. 9 shows the global visibility for a 1.8 meter radius object and a reflection coefficient $C_d = 0.5$. The visiblity constraints are a limiting magnitude of 20, elevation constraints of 0 degrees local elevation and a magnitude of the object higher than the Moon-induced background sky brightness according to the SNR constraint of $SNR = \sqrt{S/2}$ (compare Eq.7). Pink indicates visibility by at least one ground-based sensor,

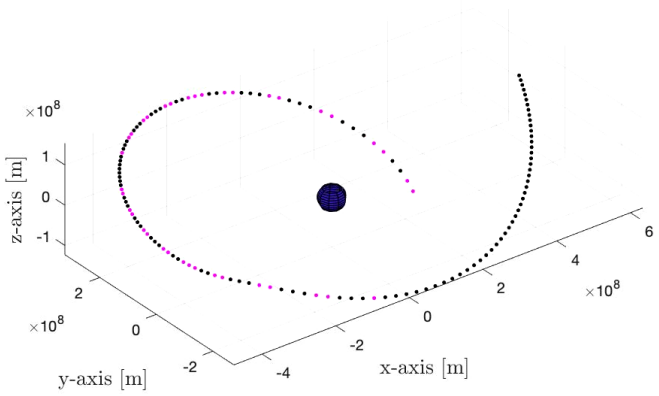

Figure 9: Trajectory of the object and visibilities for a ground-based observer with a limiting magnitude of 20 and lunar background light, for a 1.8 meter radius object and $C_d = 0.5$ and a minimum elevation of zero degrees. Ground-based sensor locations with visiblities are yellow (none present at the final time, shown here), the ones without are marked in blue (Earth size not to scale), the trajectory, for which at least one ground-based sensor has a visibility is marked pink, otherwise blue.

black indicates no sensor can provide observations on the object. Sensors are located at the center of each grid point on the Earth surface. It is obvious that even with a ground-based sensor network of sensors with excellent conditions (limiting magnitude 20), the object cannot be covered with observations towards the end of the propagation period. Observation coverage is reasonable up to this point. It can, however, again only be achieved with a global sensor network.

The Selected Transfer Orbit

This can be compared to an object in the selected transfer orbit with the same spherical object with of 3.54 meters radius, see Fig.10. with the same ground-based observer at latitude = 40.4310 degrees North and Longitude 86.9149 degrees East. Shown are the night times via gray bars and the background moon light's magnitude in the viewing direction to the object in black.

Not surprisingly, the object is bright and very well to be observed at the times when it passes by the earth, however in the far lunar passages, the magnitude increases, making it impossible for sensors with a moderate limiting magnitude to keep track of even this large object, especially when reflectivity is not absolute and smaller than 1. The moon light does interfere significantly with the observation conditions.

Fig. 11 shows the global visibility again for a 1.8 meter radius object and a reflection coefficient $C_d = 0.5$ with limiting magnitude 20. The object has to be above local horizon and an SNR constraint of values larger than $SNR = \sqrt{S/2}$ is used. One can see that the pink points, indicating visibility for at least one ground-based sensor spread throughout the orbit, same as with the black points, where not visibility for any ground based sensor, placed on the center grid points of the Earth, as shown in Fig. 11, could be determined. Please also note that the Earth is not to scale in the illustration, in order to show ground-based sensor locations more clearly. This means, even with a global sensor network, there are times, where no visibility is given and no orbit update can be computed.

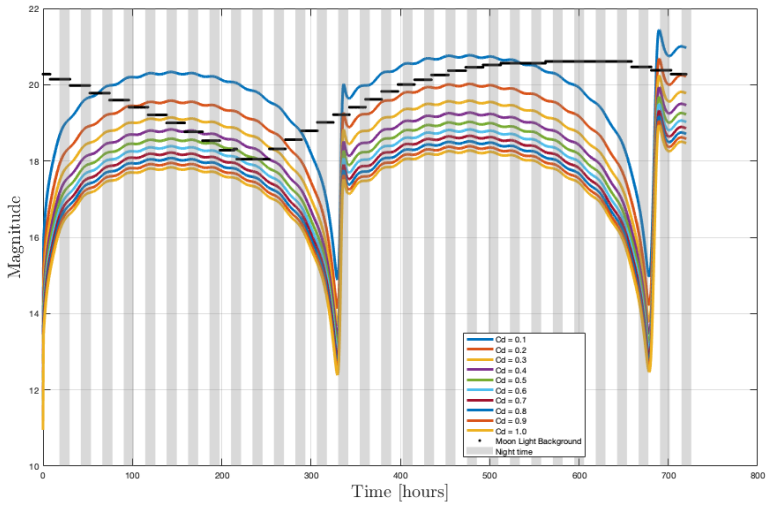

Figure 10: The selected transfer orbit: Magnitude of a one 3.54 meter radius object as a function of time with the observation location at about 40.4 deg N, 86.9 deg E.

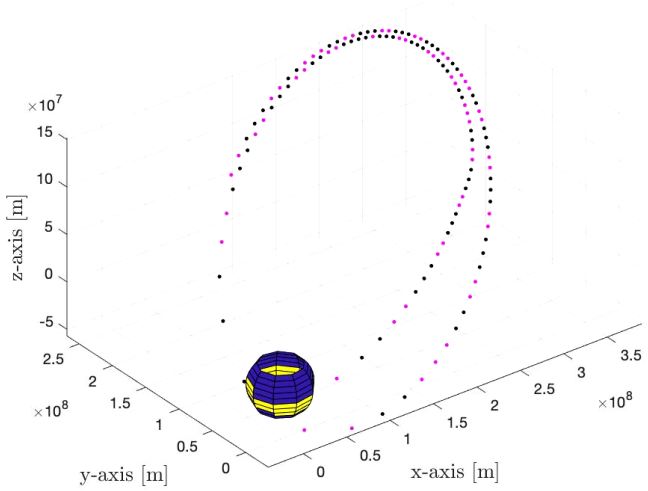

Figure 11: Trajectory of the object and visibilities for a ground-based observer with a limiting magnitude of 20 and lunar background light, for a 1.8 meter radius object and $C_d = 0.5$ and a minimum elevation of zero degrees. Ground-based sensor locations with visiblities are yellow, the ones without are marked in blue (Earth size not to scale), the trajectory, for which at least one ground-based sensor has a visibility is marked pink, otherwise blue.

UNCERTAINTY PROPAGATION

Uncertainty propagation is one of the key elements to orbit determination. Accurate propagation of uncertainty facilitates better awareness of the space environment, including improved ability to predict conjunctions/collisions and re-acquisition of previously tracked objects. A common implementation of uncertainty propagation involves propagating central moments, i.e. mean and covariance, of the distribution using elements of the extended, unscented, or quadrature Kalman filter. These approaches have inherent limitations in their ability to represent distributions that exhibit curvature or multi-modality. Recent work has expanded

upon the propagation of the central moments by introducing alternative representations of the uncertainty. The Gaussian mixture approach, pioneered in [21], for instance, has been successfully applied in a number of orbit-related applications [22, 23, 24, 25]. An additional consideration is the manner in which the state of the object is represented. Transforming the position and velocity into a set of orbital elements, such as the equinoctial orbital elements [26] or alternate equinoctial orbital elements [23], has been found to be effective in ameliorating the effects of nonlinearity on the curvature of the state distribution.

In this paper, the influence of the cislunar environment on the propagation of uncertainty, a Monte Carlo simulation is used. 1σ values of 10 m and 10 m/s are used for each channel of the position and velocity, respectively. A set of 1000 Monte Carlo trials is carried out, where the initial position and velocity are resampled for each trial, and the orbits are propagated for a duration of 30 days. The results presented here focus on relatively large initial velocity uncertainties in an effort to expose the differences in the cislunar and near-Earth environments. Again, the two numerically propagated Cartesian ephemerides models are used, the *simplified dynamics model* with the point-mass gravity of the Earth and the Sun with simplified solar ephemerides, and the *full ephemerides model* with the Earth harmonics expansion, solar, lunar and Jupiter's gravity, SRP and precise lunar and solar ephemerides.

The Selected Lyapunov Orbit

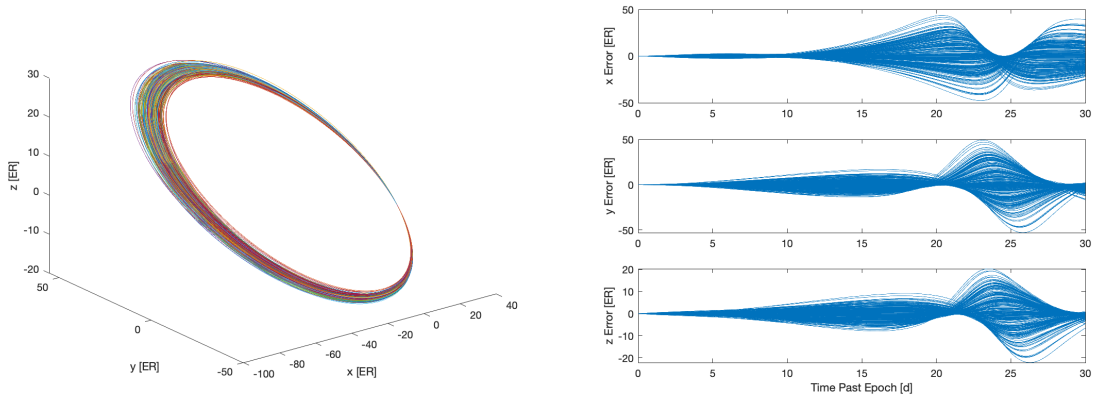

(a) Propagated orbits

(b) Position dispersions

Figure 12: Selected Lyapunov, simplified dynamics model: Propagated orbits and position dispersions for the simplified dynamics model starting from perturbed initial conditions for the Lyapunov orbit.

Monte Carlo analysis is first applied to the Lyapunov orbit, where the collection of resulting orbits for the simplified dynamics model is illustrated in Fig. 12a. This figure exhibits characteristics consistent with near-Earth uncertainty propagation, specifically in that the orbits collect together near the initial conditions and exhibit the widest spread at the opposite point along the orbits. The dispersions away from an initially unperturbed propagation are shown in Fig. 12b for the simplified dynamics model. These results illustrate that the propagation of uncertainty cannot, after a period of time, be represented by a Gaussian distribution, as the dispersions no longer exhibit symmetry (about the horizontal direction) after a period of time. To further investigate the distributional characteristics of the Monte Carlo samples, Fig. 13 illustrates projections of the individual samples along various combinations of the coordinates after 10 days, 20 days, and 30 days of propagation time. It is clearly seen that the samples progress from being reasonably Gaussian-distributed to exhibiting curvature as the propagation time increases. This is reminiscent of uncertainty propagation in the near-Earth realm. While different coordinate system selections are known to alleviate this effect, the objective here is to investigate what impact, if any, the cislunar environment has on the propagation of uncertainty.

As such, an additional Monte Carlo simulation of 1000 trials is carried out, with the only difference of now using the full ephemerides propagation model. Fig. 14a illustrates the resulting collection of trajectories.

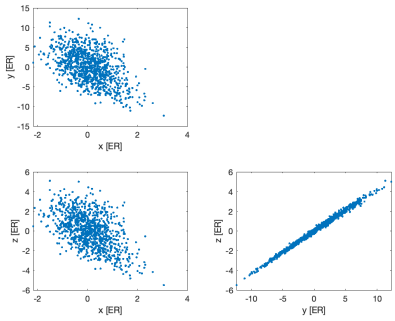

(a) After 10 Days

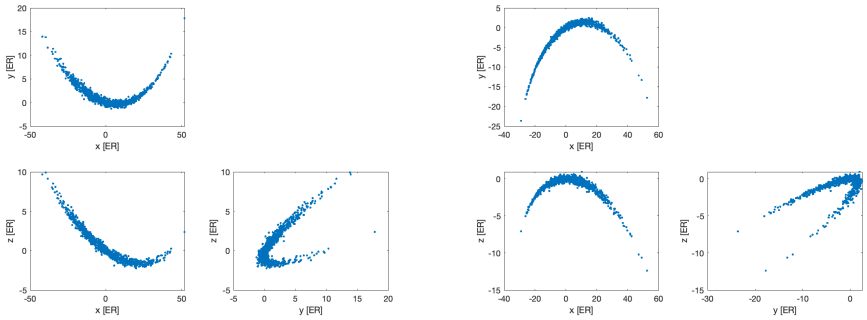

(b) After 20 Days

(c) After 30 Days

Figure 13: Selected Lyapunov, simplified dynamics model: Projections of samples onto the x-y, x-z, and y-z planes for the simplified dynamics propagation starting from perturbed initial conditions for the Lyapunov orbit.

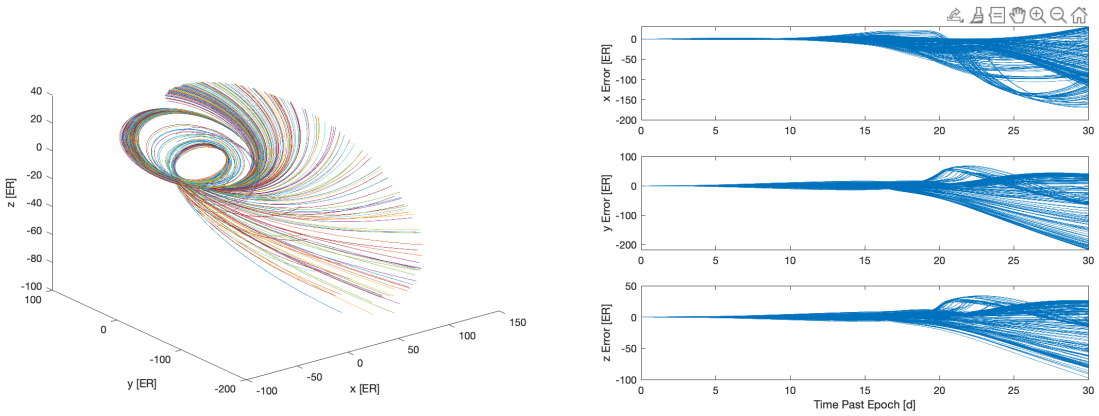

(a) Propagated orbits

(b) Position dispersions

Figure 14: Selected Lyapunov, full ephemerides model: Propagated orbits and position dispersions for the full ephemerides propagation starting from perturbed initial conditions for the Lyapunov orbit.

When comparing these results to those of Fig. 12a, it is immediately clear that the cislunar environment has a tremendous effect, introduced, for example, by the near lunar orbital passage and resulting perturbations. The position dispersions of the Monte Carlo trials with respect to an unperturbed initial condition are shown

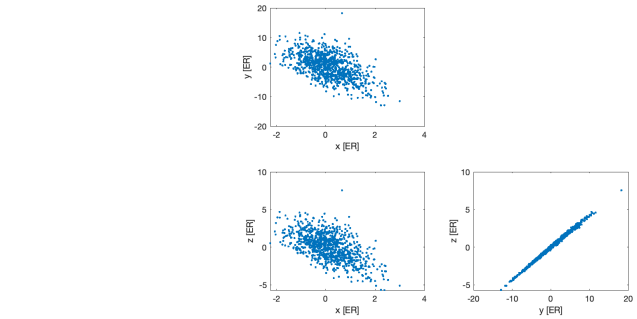

(a) After 10 Days

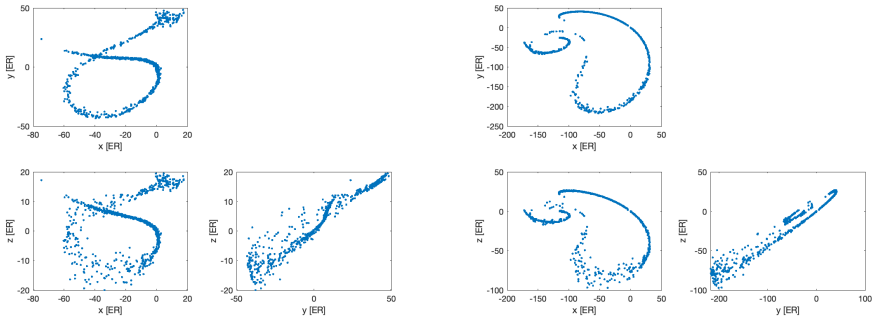

(b) After 20 Days

(c) After 30 Days

Figure 15: Selected Lyapunov, full ephemerides model: Projections of samples onto the x-y, x-z, and y-z planes for the full ephemerides propagation starting from perturbed initial conditions for the Lyapunov orbit.

in Fig. 14b, where a marked difference relative to Fig. 12b is observed. The results of Fig. 14b, much like the ones of Fig. 12b, indicate an asymmetric distribution emerges over time in the complete dynamics model; additionally, Fig. 14b shows that some clusters of trajectories begin appearing over time. To better visualize the distribution, Fig. 15 illustrates projections of the individual samples along various combinations of the coordinates after 10 days, 20 days, and 30 days of propagation time. Rather than simply being asymmetric and curved, the results of Figs. 15b and 15c indicate exceptionally complex uncertainty structures with curvatures and crossings occurring. These uncertainties are vastly different from those typically seen in the near-Earth domain. Similar to the near-Earth regime, as the initial uncertainties decrease and the initial distribution is more accurately represented by a Gaussian distribution, the propagated uncertainties remain Gaussian for a longer period of time.

Comparing the results of the simplified dynamics propagation model in Figs. 12 and 13 to the results of the full ephemerides propagation model in Figs. 14 and 15 highlights the challenges that the cislunar environment brings to bear in the estimation process. In the near-Earth regime, approaches have been developed and successfully applied to deal with distributional curvature, either using improved uncertainty models or coordinate transformations. In the cislunar domain, however, the uncertainty structure is far more complex, implying the necessity to reevaluate the efficacy of existing approaches.

The Selected DRO Orbit

Uncertainty propagation along the nominal DRO is also considered, where the results of Monte Carlo analysis are summarized in Figs. 16 and 17. These results are obtained using the full ephemerides propagation model. Figs. 16b and 17 illustrate the position dispersions away from an initially unperturbed propagation and the projections of the individual samples along various combinations of the position coordinates after

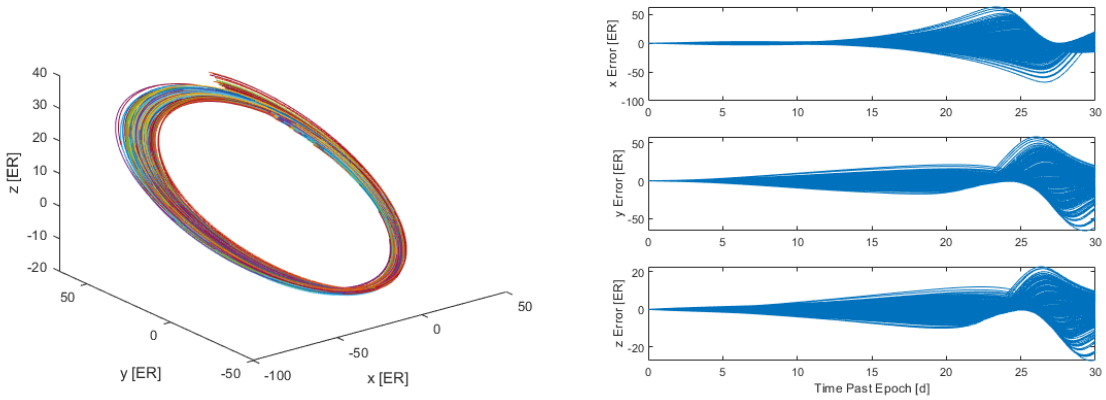

(a) Propagated orbits

(b) Position dispersions

Figure 16: Selected DRO, full ephemerides model: Propagated orbits and position dispersions for the full ephemerides propagation starting from perturbed initial conditions for the DRO.

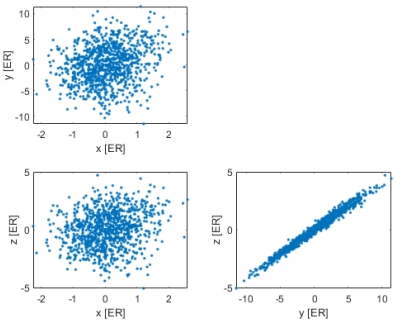

(a) After 10 Days

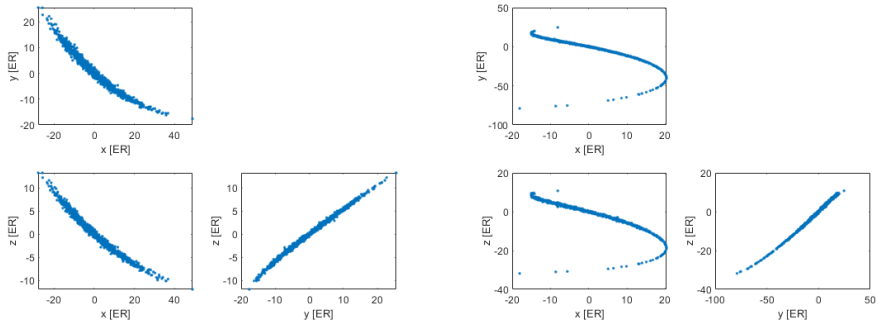

(b) After 20 Days

(c) After 30 Days

Figure 17: Selected DRO, full ephemerides model: Projections of samples onto the x-y, x-z, and y-z planes for the full ephemerides propagation starting from perturbed initial conditions for the DRO.

10 days, 20 days, and 30 days of propagation time, respectively. These results indicate that asymmetric distributions emerge after a period of time. In comparison to the results of the Lyapunov orbit, however, the degree of curvature exhibited by the DRO uncertainty propagation results is significantly less. In this manner, the results of the DRO uncertainty propagation are more in line with what is commonly expected for

uncertainty propagation in the near-Earth regime.

The Selected Transfer Orbit

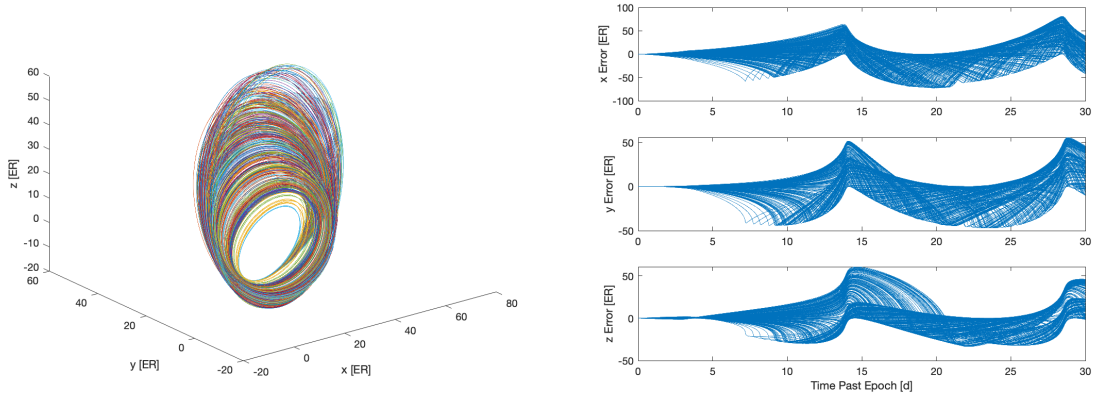

(a) Propagated orbits

(b) Position dispersions

Figure 18: Selected transfer orbit, full ephemerides model: Propagated orbits and position dispersions for the full ephemerides propagation starting from perturbed initial conditions for the transfer orbit.

As a third test case, the Monte Carlo analysis procedure is applied to the transfer orbit using the full ephemerides propagation model. Fig. 18a illustrates the resulting orbits, Fig. 18b provides the position dispersions with respect to the nominal transfer orbit, and Fig. 19 shows the projections of the individual samples along various combinations of the position coordinates after 10 days, 20 days, and 30 days of propagation time. These results demonstrate that non-Gaussian uncertainties evolve more rapidly for the transfer orbit than is observed for either the Lyapunov orbit or DRO. Unlike the Lyapunov orbit and DRO, asymmetry is already present in the position dispersion of Fig. 18b and the projected samples of Fig. 19a by 10 days of propagation time. The evolution of both the position dispersions and the sample projections beyond 10 days demonstrate an exceptionally complex uncertainty structure, similar in some regards to the one observed in the Lyapunov results of Figs. 14b and 15. Whereas the Lyapunov orbit results indicate uncertainty "crossovers" and "coils," the transfer orbit results shown here only exhibit uncertainty coils. Even though crossovers are not observed in the transfer orbit results, the coil structures are more developed than the ones observed in the Lyapunov orbit case. These results reinforce the observation that uncertainty structures in the cislunar domain can evolve in a different manner and produce different structures than are typically observed in the near-Earth domain.

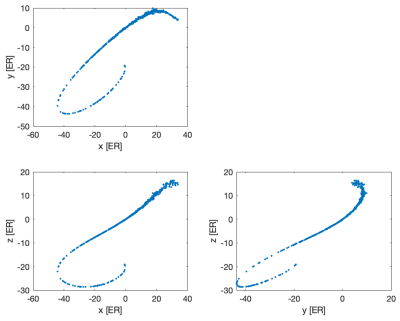

(a) After 10 Days

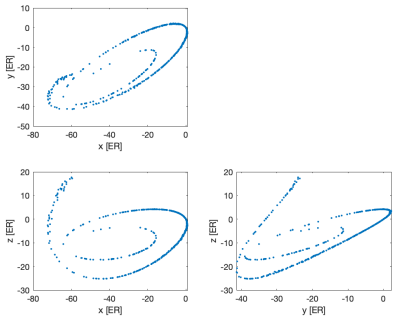

(b) After 20 Days

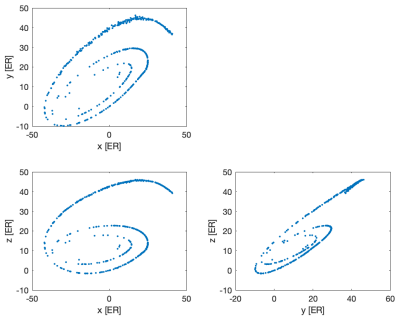

(c) After 30 Days

Figure 19: Selected transfer orbit, full ephemerides model: Projections of samples onto the x-y, x-z, and y-z planes for the full ephemerides propagation starting from perturbed initial conditions for the transfer orbit.

CONCLUSIONS

In this paper, the cislunar space situational awareness (CSSA), cislunar domain awareness (CDA) and cislunar space traffic management (CSTM) has been illustrated while focusing on a few crucial points. The acceleration dynamics in the cislunar realm is significantly different from the near-Earth environment. Hence, a simple projection of current near-Earth Space Situational, Space Domain Awareness and Space Traffic Management solutions cannot be simply successful. The number of orbital families with widely different properties is very diverse, making the orbit selection for missions, and as a result, potential locations for dead satellites and debris far from obvious.

For this paper, the popular DRO and Lyapunov families have been shown and for each a sample orbit has been selected for further investigation. In addition, a an Earth-L_2 Halo transfer orbit has been chosen. It has been illustrated that the propagation in the circular restricted three body problem is desirable for orbit selection and orbit illustration, but might be deceiving when inferring further properties. For further work with the orbits, more precise ephemerides of the other celestial bodies are needed and transformation in the inertial frame with a precise numeric propagation is desirable. Using simplified dynamics in the numeric integration provides computationally faster solutions, but can also easily lead to trajectories very far from the truth, as shown explicitly in this paper. In order to maintain some desired orbit characteristics from the circular restricted three body problem, a corrections process needs to be employed in the full ephemerides model.

Using ground-based optical sensors for the observation of objects in those aforementioned orbits faces significant challenges. Single ground stations with electro-optical sensors face large fractions of the orbits, which cannot be observed, even for large objects of several meters diameter and high reflectivity. A global network of electro-optical sensors is mandatory, even for such large objects. In this paper, however, it is

also shown that even with such a global network, depending on the orbit, large fractions might be rendered unobservable oven for those large reflective objects. This is even true for sensors of a limiting magnitude of 20. Besides the usual constraints of a minimum elevation, it turns out that background moon light also interferes with successful observations in a significant way.

Uncertainty propagation in the cislunar realm faces huge challenges, as a Monte Carlo investigation reveals. Taking the Lyapunov orbit as an example, using the simplified dynamics propagation model, a well-known banana shape uncertainty can be observed. However, the simplicity is deceiving. Employing full ephemerides propagation model leads for all investigated orbits to complicated uncertainty distributions not easily modeled with commonly applied functions even within the first orbital period.

ACKNOWLEDGMENTS

The authors would like to acknowledge the work and support of Beom Park in providing the orbits for this paper.

REFERENCES

[1] Jonathan Ruhe. SDA's Kennedy: Cislunar Space The Next Military Frontier, April, 2019. https://breakingdefense.com/2019/04/sdas-kennedy-cislunar-space-the-next-military-frontier/, last accessed at 2020-07-30.

[2] Theresa Hitchens. US Needs New Policies With Move To Cislunar: Aerospace Corp., June, 2020. https://breakingdefense.com/2020/06/us-needs-new-policies-with-move-to-cislunar-aerospace-corp/, last accessed, 2020-07-30.

[3] Air Force eyeing technology to monitor space traffic near the moon, April April, 2020. Website: space-news.com.

[4] S.R. Knister. *Evaluation Framework for Cislunar Space Domain Awareness (SDA) Systems*. Air Force Institute of Technonolgy, Wright Patterson AFB, Ohio, 2019. Master Thesis.

[5] Lynn Jenner. NASA Eyes GPS at the Moon for Artemis Missions, June 2019. http://www.nasa.gov/feature/goddard/2019/nasa-eyes-gps-at-the-moon-for-artemis-missions, last accessed 2020-07-30.

[6] Keith Scott and Christopher Krupiarz. Ccsds cislunar communications architecture. In *SpaceOps 2006 Conference*, 2006.

[7] Erin E Fowler, Stella B Hurtt, and Derek A Paley. Orbit Design for Cislunar Space Domain Awareness. In *2nd IAA Conference on Space Situational Awareness (ICSSA), Washington, District of Columbia*, 2020.

[8] Marcus J. Holzinger and Jacob K. Vendl. Cislunar periodic orbit analysis for persistent space object detection capability. In *Astrodynamics Specialist Conference, Portland, ME*, 2019.

[9] B. Banks, R.D. Smith II, V.M. Aguero R.G. Wagner, S.D. Williams, and M. Balducci M.Duncan, S. De Smet. A Sensor-Rich Solution for Lunar/Cislunar Space Domain Awareness. In *Proceedings of the 2003 AMOS Technical Conference, September 2020, Maui, Hawaii, USA*, 2020.

[10] Davide Amato, Aaron J. Rosengren, and Claudio Bombardelli. THALASSA: a fast orbit propagator for near-Earth and cislunar space. In *2018 Space Flight Mechanics Meeting*. American Institute of Aeronautics and Astronautics, 2018.

[11] M.B. Hinga. Spacebourne Orbit Determination of Unknown Satellites Using a Stabilized-Gauss-Method, Linear Perturbation Theory and Angle-Only Measurements. In *Proceedings of the 2003 AMOS Technical Conference, September 2018, Maui, Hawaii, USA*, 2018.

[12] M.B. Hinga. Cis-Lunar Autonomous Navigation via Implementation of Optical Asteroid Angle-Only Measurements. In *Proceedings of the 2003 AMOS Technical Conference, September 2020, Maui, Hawaii, USA*, 2020.

[13] C.R. McInnes. *Solar Sailing: Technology, Dynamics and Mission Applications*. Springer-Praxis, Chichester, UK, 1999. ISBN-13: 978-3540210627.

[14] A. Haapala and K.C. Howell. A Framework for Construction of Transfers Linking Periodic Libration Point Orbits in the Earth-Moon Spatial Circular Restricted Three-Body Problem. *Journal of Bifurcations and Chaos*, 26(5), 2016.

[15] D. Guzzetti, N. Bosanac, A. Haapala, K.C. Howell, and D. Folta. Rapid Trajectory Design in the Earth-Moon Ephemeris System via an Interactive Catalog of Periodic and Quasi-Periodic Orbits. *Acta Astronautic*, 126:439 – 455, 2016.

[16] A.F. Haapala, M. Vaquero, T.A. Pavlak, K.C. Howell, and D.C. Folta. Trajectory Selection Strategy for Tours in the Earth-Moon System. In *AAS/AIAA Astrodynamics Specialist Conference, Hilton Head Island, South Carolina, August 11-15*, 2013.

[17] D. Folta, T. Pavlak, A. Haapala, and K.C. Howell. Preliminary Design Considerations for Access and Operations in Earth-Moon L1/L2 Orbits. In *23rd AAS/AIAA Space Flight Mechanics Meeting, Kauai, Hawaii, February 10-14*, 2013.

[18] C. Frueh, B. Little, and J. McGraw. Optical Sensor Model and its Effects on the Design of Sensor Networks and Tracking. In *Advanced Maui Optical and Space Surveillance Technologies Conference (AMOS)*, September 2019.

[19] S.B. Howell, B. Koehn, E. Bowell, and M. Hoffman. Detection and measurement of the poorly sampled point sources imaged with 2-D arrays. *Astronomical Journal*, 112 (3):1302 – 1311, 1996.

[20] K. Krisciunas and B.E. Schaefer. A Model of the Brightness of Moonlight. *Astronomical Society of the Pacific*, 103:1033–1039, 1991.

[21] H. W. Sorenson and D. L. Alspach. Recursive Bayesian estimation using Gaussian sums. *Automatica*, 7:465–479, 1971.

[22] Gabriel Terejanu, Puneet Singla, Tarunraj Singh, and Peter Scott. Uncertainty propagation for nonlinear dynamic systems using Gaussian mixture models. *Journal of Guidance, Control, and Dynamics*, 31(6):1623–1633, November-December 2008.

[23] Joshua T. Horwood, Nathan D. Aragon, and Aubrey B. Poore. Gaussian sum filters for space surveillance: Theory and simulations. *Journal of Guidance, Control, and Dynamics*, 34(6):1839–1851, November-December 2011.

[24] K.J. DeMars and M. Jah. Probabilistic initial orbit determination using radar returns. In *Proceedings of the AAS/AIAA Astrodynamics Specialist Conference Hilton Head*, 2013.

[25] Vivek Vittaldev, Richard Linares, and Ryan P Russell. Spacecraft uncertainty propagation using gaussian mixture models and polynomial chaos expansions. *Journal of Guidance, Control, and Dynamics*, 39(9):2163–2169, 2016.

[26] R. A. Broucke and P. J. Cefola. On the equinoctial orbit elements. *Celestial Mechanics*, 5:303–310, May 1972.